Magnetic Silica Nanoparticle Cellular Uptake and Cytotoxicity Regulated by Electrostatic Polyelectrolytes–DNA Loading at Their Surface

Ana B. Davila-Ibanez,[†] Veronica Salgueirino,[†,*] Vicenta Martinez-Zorzano,[‡] Rosalia Mariño-Fernández,[†] Andres García-Lorenzo,[‡] Melodie Maceira-Campos,[†] Monica Muñoz-Ubeda,[§] Elena Junquera,[§] Emilio Aicart,[§] Jose Rivas,[⊥] F. Javier Rodriguez-Berrocal,[‡] and Jose L. Legido[†]

[†]Departamento de Física Aplicada, Universidade de Vigo, 36310, Vigo, Spain, [‡]Departamento de Bioquímica, Genética e Inmunología, Universidade de Vigo, 36310, Vigo, Spain, [§]Departamento de Química-Física, Universidad Complutense de Madrid, 28040, Madrid, Spain, and [⊥]INL, International Iberian Nanotechnology Laboratory, 4715-330 Braga, Portugal

The potential of nanomaterials for drug delivery and related therapies has been extensively explored in recent years.[1] The possibilities become enhanced in the case of magnetic nanoparticles[2] since they can be additionally used for imaging, diagnosis, hyperthermia, and cell separation when considering the advantage of an external magnetic manipulation.[3,4] Targeted delivery and controlled release of drugs to any type of cells or specific organ would potentially maximize its therapeutic efficacy while minimizing the side effects.[5] Consequently, administering safe and effective therapy that is lesion-specific and with few side effects necessitates the integration of nanotechnology with molecular biology and medical sciences, and the challenges are not minor.[6]

Nanostructures of different size, shape, and composition have many applications in biomedical imaging, clinical diagnostics, and therapeutics. These nanostructures when biofunctionalized can indeed resemble biomolecules and biomolecular assemblies in terms of size and chemical composition and sometimes even function.[7] This "nano–bio" interface comprises therefore the dynamic physicochemical interactions, the kinetics, and the thermodynamic exchanges between the nanomaterials' surface and biological components such as phospholipids, endocytic vesicles, organelles, DNA, or biological fluids.[8] Its ability to recruit the nanostructures and multivalently bond them to surface receptor(s) is crucial to enhance specific affinity, reduce nonspecific interactions, and direct receptor-mediated endocytosis, all of

ABSTRACT
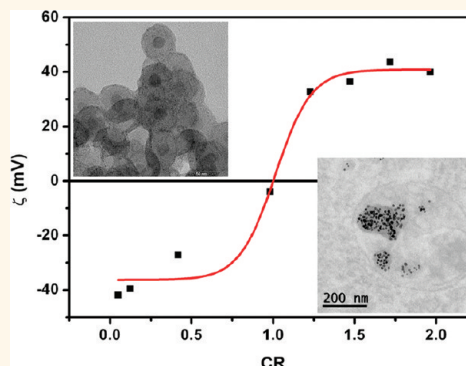
Magnetic silica nanoparticles show great promise for drug delivery. The major advantages correspond to their magnetic nature and ease of biofunctionalization, which favors their ability to interact with cells and tissues. We have prepared magnetic silica nanoparticles with DNA fragments attached on their previously polyelectrolyte-primed surface. The remarkable feature of these materials is the compromise between the positive charges of the polyelectrolytes and the negative charges of the DNA. This dual-agent formulation dramatically changes the overall cytotoxicity and chemical degradation of the nanoparticles, revealing the key role that surface functionalization plays in regulating the mechanisms involved.

KEYWORDS: polyelectrolytes · DNA compaction · magnetoplexes · cellular uptake · cytotoxicity

which would then maximize a selective delivery of cargo.[9] However, in spite of what has been achieved so far, a complete understanding of how cells interact with nanostructures at the molecular level remains poorly understood. Indeed, despite the many reports about cytotoxicity and biocompatibility, synthetic routes of nanoparticles intended

to specifically interact with cells are lacking and largely unappreciated, and consequently, few attempts to link the cellular responses to the physicochemical properties of the engineered nanoparticles have been reported.[8]

One of the most challenging biological barriers to overcome is the cell membrane. In this regard, it is necessary to develop an internalization strategy for nanostructures (considering the regulated portals of entry into the cell[10]) that can generate or favor an effective delivery. The best-described mechanism of cellular entry is endocytosis, referring to a two-step energy-dependent uptake process in which the nanomaterial is first engulfed in pinched-off vesicles (endosomes) that carry the ingested material into the cellular interior and then is rapidly digested through acidification (lysosomes).[11,12] Ashley et al. have shown the process of internalization to be dependent on the nanocarrier size, with 50 nm carriers being most efficiently internalized (1800 particles/cell).[9] These results provided evidence that internalization occurs through this endocytotic pathway, given that membrane wrapping occurs most efficiently for particles 30−60 nm in diameter.[13] Since nanoparticles appear however inherently and nonselectively to be passing through the cell membrane, understanding this aspect will be key to designing the most selective and therefore effective chemotherapeutic platforms with the very important perspective of simultaneous nanoparticle cellular uptake and cytotoxicity.[14,15]

Synthetic nanoparticles (unless with very small dimensions) cannot pass through the cell membrane without disrupting its integrity. Charged nanoparticles for example induce transient poration of cell membranes to enter, but it is a process also associated with cytotoxicity.[16] Therefore the surface properties of nanomaterials play a critical role in determining the outcome of these interactions,[17] and the new approaches should enable enhancing nanoparticles cell internalization at low to moderate concentrations but with greatly enhanced uptake.[18] As mentioned, these nanostructures should resemble biomolecular assemblies in order to benefit their interactions with cells. In this context, the unique chemical and scaffolding properties provided by single- or double-stranded DNA fragments can establish the necessary synergy with the nanoparticles for assembling and testing the different mechanisms involved.[19] For example, mesoporous silica supports were reported to trigger cargo release involving these biomolecules.[20]

DNA characteristics such as biocompatibility, ability to self-assemble in a very predictable manner, or controlled length and sequence render them very convenient molecules for biorelated applications where magnetic nanoparticles can be exploited. We propose therefore the use of magnetic nanoparticles as multicomponent chemotherapy agents, in view of potential synergistic drug- and magnetism-based activities.

Accordingly, we have prepared magnetic silica nanoparticles with DNA fragments attached on a polyelectrolyte-primed surface and that are very stable in aqueous solution. This surface functionalization with the DNA fragments establishes the necessary synergy with the nanoparticles, in order to help them resemble biomolecular assemblies. We can additionally exert control over the surface charge to define the ζ-potential necessary to get through the cell membranes, by means of a compromise between the positive charges of polyelectrolytes and the negative charges of the DNA fragments. This dual-agent formulation can supply efficient internalization in cells, can influence the chemical degradation mechanisms of the cells, and consequently alter the cytotoxicity results. The findings presented here may assist in the design of nanoscale delivery and therapeutic systems and provide insights into nanotoxicity.

RESULTS AND DISCUSSION

Magnetic Silica Nanoparticles (MSNs). Fe_3O_4 (6.6, 12.8, and 15 nm) and $CoFe_2O_4$ (8.1 and 21.5 nm) magnetic cores were incorporated in silica nanoparticles by the reverse microemulsion method optimized by Koole et al. for semiconductor quantum dots.[21] The magnetic cores were transferred to chloroform (those from the thermal decomposition synthesis) or dispersed in cyclohexane (the cobalt ferrite nanoparticles synthesized in aqueous solution by co-precipitation) before addition to the microemulsion system. The initial amount of magnetic cores was optimized in every case before the shell growth. In all the cases, the resulting magnetic silica nanoparticles of different final diameter have one magnetic nanoparticle incorporated exactly in the center of the nanoparticle. The control over the number of magnetic cores per silica particle is high: 95% of the particles contain a single magnetic core, around 4% are empty, and less than 1% contain more than one core. These percents roughly vary among the samples analyzed, although the percentage of nanoparticles with one single core increases as the size of the magnetic material to be coated is increased. The mechanism reported by Koole et al. for semiconductor quantum dots[21] suggests that the NP-5 molecules attached to the quantum dots surface may be driving the silica coating, by replacing the ligands at the surface (the oleic acid molecules used in our case). As also pointed by Koole and co-workers,[21] the better coating depends on the strength of the ligands when binding to the surface of the nanoparticles since a stronger binding reduces the ligand exchange and hinders the silica coating. In our case, we can think about the larger curvature of the bigger nanoparticles, which may render easier the oleic acid ligand exchange required and would explain the better results of silica coating in the larger sizes. The major challenge in this step is the
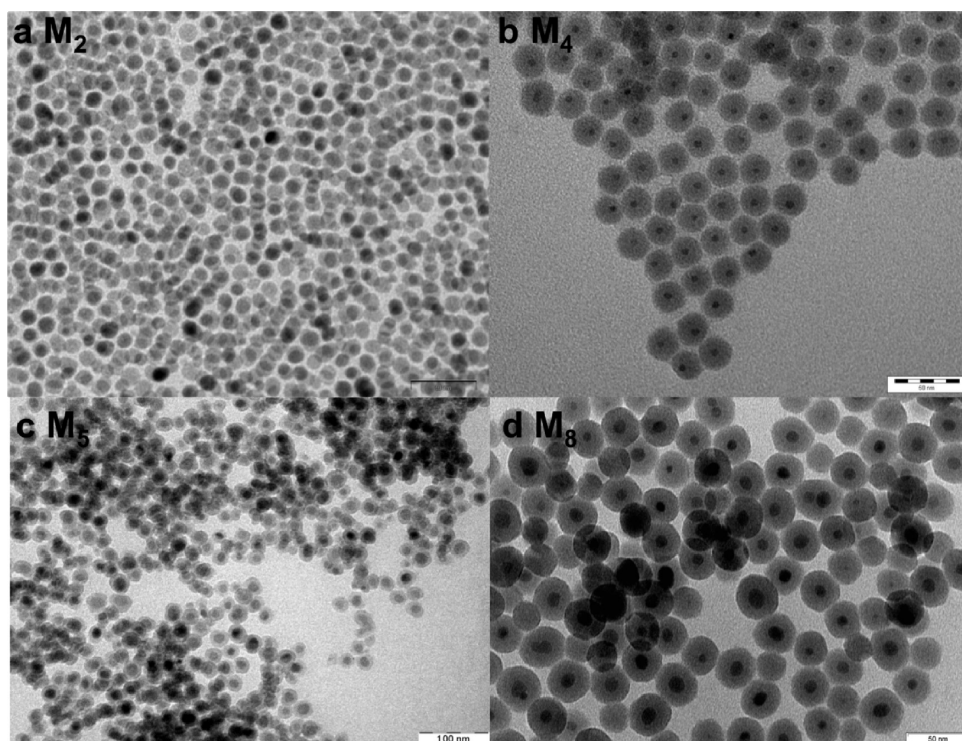
Figure 1. TEM images of 12.8 nm magnetite nanoparticles (sample M_2) (a) and of MSN (Fe_3O_4@SiO_2 nanoparticles) from samples M_4, M_5, and M_8, with different core size and shell thickness (b, c, and d) (scale bar: 50 nm in a, b, and d and 100 nm in c).

formation of core—shell particles that are largely uniform in core size and shell thickness. This controlled microemulsion-based silica coating is therefore very convenient because the nanoparticles produced maintain uniformity and the method itself is very reproducible.

Figure 1a includes a TEM image of 12.8 nm Fe_3O_4 nanoparticles, without silica (M_2, see Table 1, Supporting Information). Figure 1b, c, and d show TEM images of magnetite-based MSNs: 6.6 nm magnetite nanocrystals coated with an 8.8 nm thick silica shell (M_4) (b), 15 nm magnetite nanocrystals coated with a 4.7 nm thick silica shell (M_5) (c), and 12.8 nm magnetite nanocrystals coated with a 9.7 nm thick silica shell (M_8) (d). Figure 2 shows TEM images of 8.1 nm $CoFe_2O_4$ nanoparticles (C_1) without silica (a) and 21.5 nm $CoFe_2O_4$ nanoparticles coated with a 9.5 nm thick silica shell (C_5) (b).

Table 1 (SI) summarizes the samples of magnetic nanoparticles and MSNs synthesized using this microemulsion process, detailing the magnetic material and size of the core, the final diameter, and the silica shell thickness. This table also includes the number of layers of polyelectrolyte wrapped around the nanoparticles and the ζ-potential after the polyelectrolyte deposition, described later. The samples are denoted as M in the case of magnetite based, and C in the case of cobalt ferrite-based MSNs. The subindex of every sample name correlates with the final diameter; that is, the larger the subindex, the larger the nanoparticles. Table 1 (SI) reflects the ability to tune the final size of the resulting core—shell nanoparticles and their low polydispersity.

In view of this tuning of the silica shell thickness when coating the different magnetic cores employed, Table 1 (SI) also indicates the excellent reproducibility of the process exploited.

The range of sizes attained determines the available specific magnetic characteristics (depending mainly on the magnetic core material and dimensions but also on the silica shell thickness, which contributes to decrease the saturation magnetization of the sample in emu/g and reduces the interactions between the nanoparticles), which will specify their potential biorelated applications. Consequently, it is also worthy to underline the very stable core—shell morphology accomplished, which favors nanoparticle purification after each step of functionalization and in physiological conditions.

All the samples summarized in Table 1 (SI) are magnetic due to their core of magnetite or cobalt ferrite, which means that they can be manipulated by an external magnetic field gradient (a magnetic field gradient is required to exert a force at a distance since a uniform field would give rise to a torque but not to translational action[22]). The nanoparticles were therefore chosen in view of the magnetic properties displayed. Although many reports have been published on the synthesis of low-dimensional magnetic materials in high yields, it is still important to underline those strategies that enable control over the magnetic response. In these ferrimagnetic spinel (MFe_2O_4; M = Fe, Co) nanoparticles, we found hysteresis that corresponds to
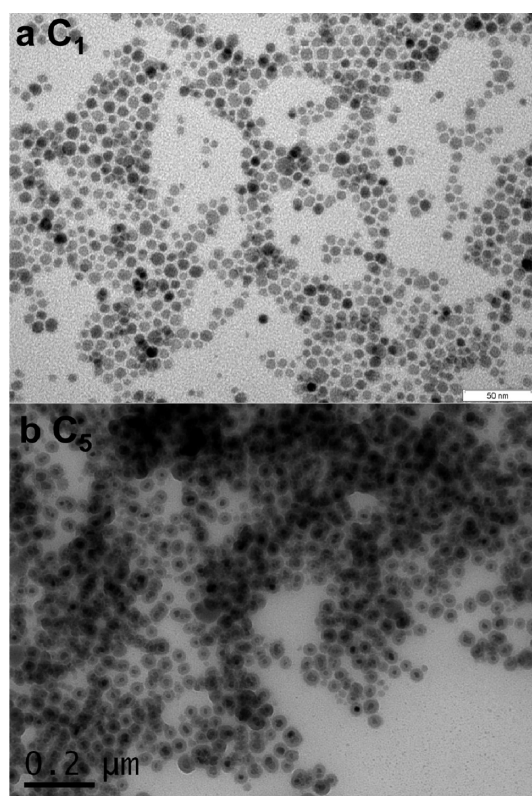
Figure 2. TEM images of 8.1 nm cobalt ferrite nanoparticles (sample C_1) (a) and of MSNs (CoFe$_2$O$_4$@SiO$_2$ nanoparticles) from sample C_5 (b) (scale bar: 50 nm in a and 200 nm in b).

irreversibility in the magnetization process. The shape of these loops is mainly determined by temperature, composition, and particle size.[23] We have chosen to magnetically characterize the smaller magnetite and the larger cobalt ferrite nanoparticles, in order to appreciate the range of different and reachable magnetic behaviors using the nanoparticles included in Table 1 (SI). The dc magnetic properties of the nanoparticles were recorded in a SQUID magnetometer, at 300 K (considering their potential biorelated applications) (Figure 3a and b) and as a function of temperature (ZFC-FC curves) (Figure 3c), since they provide information on energy barriers for magnetization reversal. Figure 3a and b show the hysteresis curves collected at 300 K (at lower fields in b) and underline the room-temperature superparamagnetic behavior of the 6.6 nm magnetite nanoparticles (which show the anhysteretic but still sigmoidal M−H curve) and the ferromagnetic-like behavior of the 21.5 nm cobalt ferrite nanoparticles (characterized by the hysteresis loop with coercive field $H_C = 340$ Oe). The smaller particles offer a single domain ground state, which leads to superparamagnetism, where the magnetic moment of the particles as a whole is free to fluctuate in response to thermal energy, while the individual atomic moments maintain their ordered state relative to each other. The cobalt ferrite nanoparticles on the contrary offer an open hysteresis loop that is associated with the magnetothermal irreversibility

processes and reflects the energy necessary to overcome the barrier to domain wall motion and/or the magnetization reversal, imposed by their intrinsic anisotropy and grain boundaries in the material. This energy delivered by the applied field is proportional to the area enclosed by the hysteresis loop. Furthermore, if applying a time-varying magnetic field to this material, one can establish a constant flow of energy into the nanoparticles, which would be transferred as thermal energy to the surroundings.[3] Figure 3c shows the temperature dependence of the magnetization of the magnetite and cobalt ferrite nanoparticles under zero-field-cooled (ZFC) and field-cooled (FC) conditions ($H = 100$ Oe). The irreversibility (i.e., splitting between the FC and ZFC curves) observed increases upon shifting from magnetite to cobalt ferrite. The ZFC and FC curves are irreversible at a temperature quite close to the maximum shown in the ZFC conditions, likely due to the relatively narrow size distribution of the magnetite nanoparticles. Regarding the cobalt ferrite nanoparticles, over the whole temperature range, the FC curve yields a larger magnetization and approaches the value of the ZFC magnetization only above 325 K. The ZFC curve of these larger nanoparticles increases monotonically up to 325 K. The observed joining of the ZFC−FC curves let us know that the nanoparticles behave as ferrimagnets ($T < T_C$), ensuring nonzero coercivity values, in accordance with the hysteresis shown at 300 K.

In all cases, the MSNs can be separated from their medium by passing the fluid mixture through a region in which there is a magnetic field gradient that can immobilize the tagged material via the magnetic force exerted. This force will need to overcome the hydrodynamic drag force acting on the magnetic particle in the flowing solution, directly dependent on the size of the particles, on their surface chemistry, and on the viscosity of the medium.[24] This physical principle gains importance in these cases because it also governs, for example, the drug delivery, guiding the magnetic drug carriers to target specific sites. This more efficient localized targeting of the drug reduces the amount of systemic distribution of the cytotoxic drug and consequently the associated side effects and the dosage required.

DNA Compaction. Understanding the influence of the nanoparticle surface chemistry on their interactions with the cell membrane and cytoplasm certainly facilitates the fundamental understanding of their unique physicochemical behavior for potential in vitro and in vivo studies. Polycationic polymers have been reported to exhibit substantial membrane disruption behavior including nanoscale hole formation, contrary to the neutral ones over a similar concentration range.[15] This ability of cationic polymers to disrupt the cell membrane is very important from a biological perspective since it permits reaching the cytoplasm and the
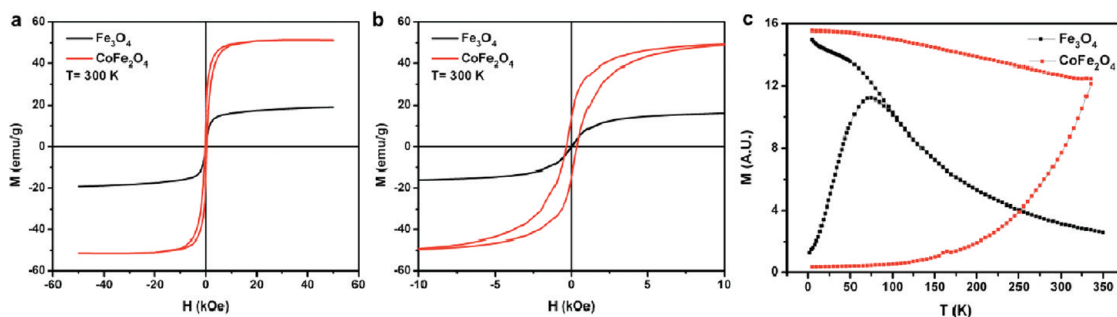
Figure 3. Magnetic hysteresis loops at 300 K (a, b) and zero-field-cooled (ZFC) and field-cooled (FC) magnetization curves at 100 Oe (c) of the nanoparticles from samples M_1 and C_2. Magnetization is shown in emu/g of sample (magnetic material + silica).

different organelles. A large number of references have reported the ability of cationic colloidal aggregates, either liposomes or micelles, to also compact DNA chains, thus forming lipoplexes or surfoplexes, respectively, by means of an entropically favored electrostatic interaction.[25−33] Other cationic agents have been employed as well for DNA compaction, such as cationic peptides and proteins or cationic polyelectrolytes,[34,35] and Zinchenko et al. and later Rosa et al. studied the physical chemistry of this association but between cationic nanoparticles and DNA.[36,37] The compaction of long duplex DNA by cationic nanoparticles has been systematically studied, regarding the effect of salt concentration, particle size, and particle charge by means of single-molecule observations from fluorescence and TEM. This DNA compaction was found to proceed through the formation of structures of different morphologies with the amount of DNA adsorbed per particle depending weakly on nanoparticle concentration but strongly on particle size and being optimal at an intermediate salt concentration. Three different complexation mechanisms were proposed: free DNA adsorption onto the nanoparticle surface, DNA wrapping around the nanoparticles, and nanoparticles fixed along the DNA chains.[36,38]

Analogously, we propose this kind of interaction using the MSNs already introduced but positively charged. The hydroxide ions present at the MSN surface render them negatively charged at neutral pH. Accordingly, we have exploited the common layer-by-layer (LbL) self-assembly technique to drive polyelectrolytes (PEs) such that we can reverse the MSNs' net surface charge. The method consists of depositing a precursor multilayer PE film alternating PDADMAC (poly(diallyldimethylammonium chloride)) and PSS (poly(sodium 4-styrenesulfonate)) onto the MSNs, to generate a uniform surface charge and smooth coating.[39−41] Driven by electrostatic interactions, positively charged PDADMAC and negatively charged PSS were therefore alternatively deposited onto the surface of the MSNs, forming a uniformly charged PE film with one, three, or five layers. This process was followed and characterized by zeta-potential (ζ) measurements (see Table 1 (SI)). The initial and negative values of the ζ-potential of the MSNs without any functionalization at neutral pH are relatively large (30−50 mV), ensuring the nanoparticles' colloidal stability. The absolute values of ζ-potential slightly vary upon increasing the number of layers of PE deposited but reverse the charge, consequently improving the colloidal stability and confirming the successful PE functionalization. The direct consequence corresponds to the homogeneous distribution of charges in the surface of the nanoparticles after the PE film deposition, which leads to the further compaction of DNA.[42]

Consequently, negatively charged DNA fragments were further compacted on the PE-functionalized MSNs. The DNA fragments are assembled by means of the electrostatic interactions between the negatively charged phosphate groups of the DNA and the positive charges belonging to the outer layer of the PDADMAC. According to Zinchenko and co-workers and considering the total diameter of the MSNs employed and the average 2700 bp per DNA fragment, it seems feasible to have a DNA wrapping effect around the nanoparticles.[36]

In order to check for any morphological or structural effect on the MSNs after deposition of the odd number of layers of polyelectrolytes and the outer layer of DNA fragments, transmission electron microscopy (TEM) characterization was carried out. Figure 4 shows TEM images of the MSNs from sample M_8 after the multilayered film deposition. Figure 4a shows the individual MSNs, functionalized with three layers of PEs (PDADMAC/PSS/PDADMAC), which form some bridges between the individual beads, likely caused by the strong interactions established in between as the solvent evaporates during the preparation of the TEM grid. In order to check the viability of the next step to compact the DNA helixes onto the positively charged surface, the MSNs were additionally incubated in a phosphotungstic acid solution (10% vol $H_3PW_{12}O_{40}$), widely used as a negative stain.[43] The phosphotungstic acid molecules are known to combine with ester groups, for example, with the carboxylic ones on the
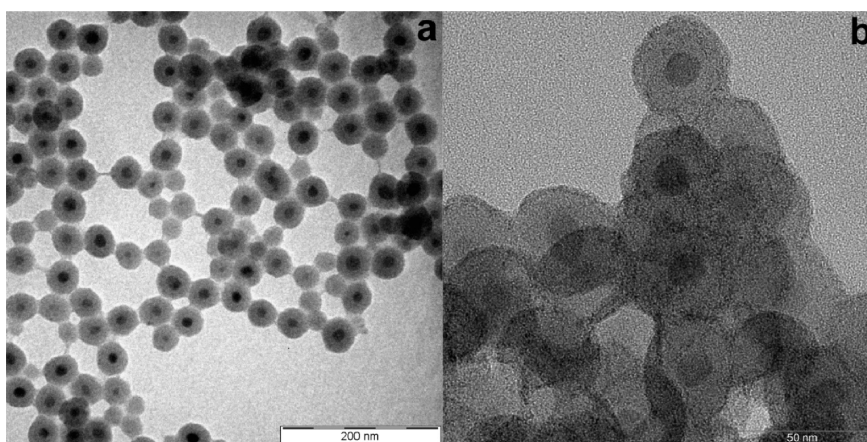
Figure 4. TEM images of MSNs from sample M_8 coated with three layers of polyelectrolytes (a) and an extra layer of DNA fragments after interacting with phosphotungstic acid molecules acting as a negative stain (b).
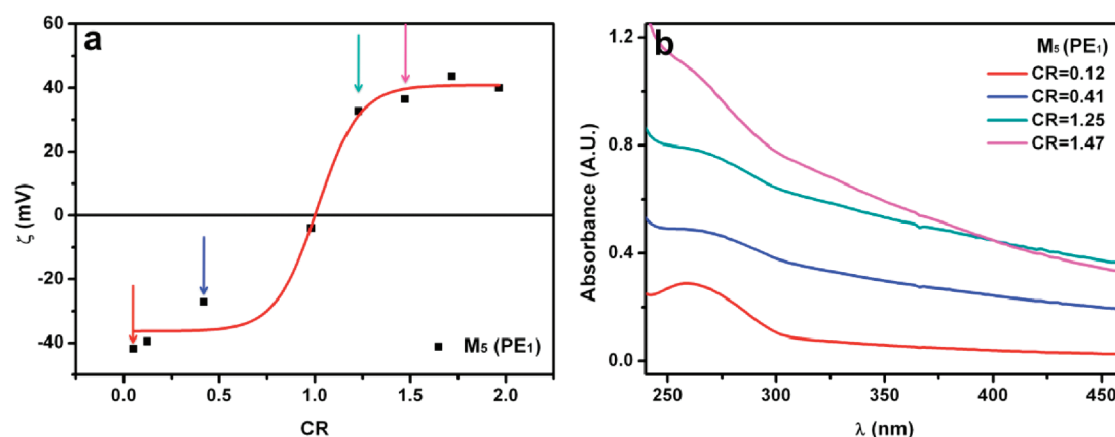

Figure 5. Sigmoidal ζ-potential dependence (a) and UV–vis spectra (b) upon adding different amounts of MSNs from sample M_5 to a constant volume of the DNA solution in separate experiments.

poly(2-(methacryloyloxy)ethylphosphorylcholine)-co-poly-(2-(diisopropylamino)ethyl methacrylate[12] or with the phosphate ester groups from the DNA fragments, as in this case. The mechanism of adsorption has been proposed as being electrostatic rather than involving hydrogen bonding.[44] This dye permits therefore increasing the electronic contrast of the MSNs upon interaction with the DNA helixes compacted at their outer surface due to the propensity of the metal–oxygen framework to accommodate excess electrons.[45] Figure 4b shows a TEM image of the magnetoplexes (MSNs–DNA complexes) once incubated in the phosphotungstic acid solution. This interaction with the phosphotungstic cations slightly increases the electronic contrast at their outer surface. The dye loading is indeed concentrated in the outer concentric area of the nanoparticles' surface, since the phosphotungstic cations have reacted with the phosphate ester groups present in the DNA helixes. This increased electron density arises from the tungsten atoms (atomic number of 74) present in the dye molecules

and confirms therefore the DNA fragments' deposition and wrapping around the nanoparticles.

ζ-Potential measurements help to characterize the physicochemical properties at the surface of the nanostructures employed in this study. Since the electrostatic interactions at the nanoparticles' surface are the driving force for the DNA compaction process, the resultant surface charge and the consequent ζ-potential may help to illustrate the magnetoplex formation. Figure 5 includes the variation of the ζ-potential value (a) and UV–vis spectra (b), upon adding appropriate amounts of MSNs (sample M_5, just one layer of PDADMAC polyelectrolyte) to 0.5 mL of stock solution of DNA, whose concentration is kept constant, in order to cover a wide range of charge ratio (CR = moles of the MSNs' positive charges/mol of DNA negative charges). ζ-Potential follows a sigmoidal curve upon varying the MSNs/DNA ratio that clearly reflects the charge inversion below and above the isoneutrality. This isoneutrality situation is defined as the charge ratio at which the negative charges of DNA are stoichiometrically balanced by the positive charges of the PDADMAC
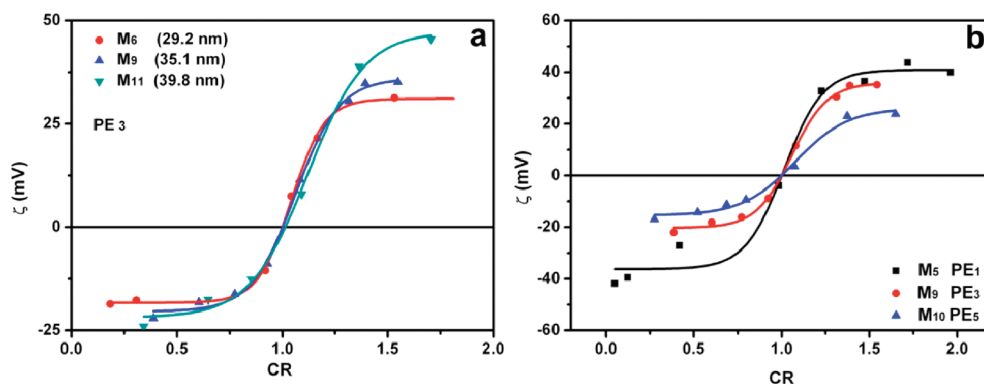
Figure 6. Sigmoidal fitting of the ζ-potential as a function of CR varying the diameter of the nanoparticles (a) and the layers of polyelectrolytes (b), upon adding a different amount of MSNs to a constant volume of the DNA solution.

located at the surface of the MSNs ($\zeta = 0$ mV; CR = 1). This trend with the three different regions corresponds to (a) the region where the net charge is negative (excess of DNA molecules) and almost constant, (b) the region where the inversion of ζ-potential sign takes place, and (c) the region where the net charge of the magnetoplexes is positive and tends to the value of the initially measured ζ-potential in aqueous solution (excess of MSNs and, therefore, lower amounts of DNA fragments attached). Notice that this is the region of potential interest for cellular transfection purposes, given that the net positive charge is compatible with the negatively charged cellular membrane. Close to iso-neutrality, however, the colloidal stability of the nanoparticles, determined by their surface charge, becomes compromised.

Figure 5b includes UV−vis spectra of the solutions obtained by mixing independently different proportions of MSNs and DNA, offering therefore different CR values. Accordingly, one can also observe some changes in the absorption, mainly related to the fact that the presence of the nanoparticles in solution importantly increases the scattering effect and screens the DNA absorbance maximum (located at $\lambda \approx 260$ nm). Additionally, the electrostatic interactions established may also lead the DNA fragments to trap more than one nanoparticle. In that case, bigger aggregates scatter more light and can even precipitate, reducing the DNA absorption upon removing the fragments from the solution.

The variation of ζ-potential was fitted to the sigmoidal trend already mentioned, analogously to that for other complexes using colloidal aggregates.[25,32] This trend is reproducible in all the MSN samples, although some cases fit better the sigmoidal curve, depending mainly on the magnetoplexes' conformation when close to isoneutrality (lower colloidal stability).

Figure 6 shows representative plots of ζ-potential *vs* CR for samples M_6, M_9, and M_{11}, all with three layers but changing sizes from 29.2 to 35.1 and to 39.8 nm (MSN average diameter) (a), and for samples M_5, M_9, and M_{10}, with one, three, and five layers of polyelectrolytes

alternating PDADMAC and PSS (b), with the aim of underlining the nondependence in terms of size (at least in the range considered), but the importance of the number of layers. Thus, the first case, all samples with three layers of polyelectrolytes, emphasizes the reproducibility of the sigmoidal curves, all with a very similar slope independent of the size of the nanoparticles employed.

In the second case, however, we first have to remark that the samples showed average ζ-potentials of 44.9, 54.5, and 41.3 mV, respectively, before mixing the nanoparticles with the DNA. These initial average ζ-potential values stem from the different size (24.4, 35.1, and 38.2 nm) and from the different number of layers of polyelectrolytes (one, three, and five layers). The important issue now is that although the general behavior is similar, the number of polyelectrolyte layers seems very important when fitting the ζ-potential to vary sigmoidally with CR, obtaining a less satisfactory result when only one layer of polyelectrolyte was previously deposited onto the nanoparticles. The improvement in the electrostatic behavior as increasing from one to three or five layers of polyelectrolytes can be clearly appreciated, independently of the fact that we have also changed the size, which in view of Figure 6a does not exert an important influence.

The optimum morphology of the resulting complexes, in the case of liposomes for example, depends on the fluidity of the lipidic membrane and the surface charge density, related to the nature, concentration, and composition of the cationic-zwitterionic lipid mixture, pH, temperature, and ionic strength.[46] In this case, however, the whole structure is not that flexible since the cationic substrate corresponds to the rigid inorganic nanoparticles. Therefore, the arrangement of the DNA fragments on the surface of the nanoparticles will depend on the direct relation between DNA segment length and nanoparticle size. In the relatively narrow range of sizes employed in this investigation and considering the average 2700 bp per DNA fragment of CT DNA used, the DNA chains adsorb on the particle surface (wrapping), increasing the ribbed texture given

by the previous polyelectrolyte film multilayer. Considering the TEM images of nanoparticles obtained using the phosphotungstenic acid, the adsorbed DNA turns around the nanoparticles, wrapping them. In solution, however, the PE film jointly with the DNA fragments spread outward, increasing the hydrodynamic radius of the magnetoplexes obtained.

In Vitro Cellular Uptake. To characterize the interactions between cells and the magnetoplexes formed, the Caco-2 cell line was used to monitor the internalization pathway and to evaluate their cytotoxicity. Cell viability of magnetoplexes-treated cells was measured and expressed as a percentage compared to that of untreated cells. Among the magnetoplexes tested, only certain cases were efficiently internalized by cells and localized to the endolysosomal compartments after 24 h of incubation at 37 °C. Because of that, in the physiological conditions encountered by the magnetoplexes upon crossing the cell membrane, different chemical processes can initialize. Previous studies have shown that cells can take up nanoparticles *via* endocytosis pathways and degrade them into lysosomes.[47] During this cellular endocytosis, nanoparticles experience a decrease of pH, from that of the extracellular medium (7–7.5), to early and late endosomes (6–5.5), to the acidic environment of lysosomes (4.5–4.8). In the lysosomes, nanoparticles may be exposed to the combined effect of acidic pH and lysosomal hydrolases (enzymes that can hydrolyze proteins, DNA, RNA, polysaccharides, and lipids).

The magnetoplexes' chemical and colloidal stability is crucial in these experiments, and therefore we avoid the isoneutrality situation (CR = 1) at their surface. Additionally, since relevant to the present study and depending on the number of DNA fragments attached, the MSNs should present a significant amount of free cationic functional groups from the PDADMAC, allowing average positively charged magnetoplexes to facilitate the interactions with the cell membrane. In order to fulfill this requirement, we have used magnetoplexes with CR > 1, located in the intermedium (CR $\in$ (1, 1.5)) or in the positive, almost constant (CR > 1.5) ζ-potential range in the sigmoidal curve. Magnetoplexes with CR < 1 were not used in these experiments.

In order to compare different cases of magnetoplexes, we employed the samples summarized in Figure 7: M_8, M_{12}, and M_{14} with a sufficient DNA loading so that we have magnetoplexes with CR $\in$ (1, 1.5), and M_5, M_6, M_{14}, and C_4 with less DNA loading so that we have magnetoplexes with CR > 1.5. The first type of magnetoplexes (CR $\in$ (1, 1.5)) did not internalize the cell membranes. We attribute this behavior to the fact that the near-neutral surface charge decreases their colloidal stability and can likely lead to aggregation when injected in the cell culture, rendering very difficult the endocytosis of the larger composites formed. Because they are unable to interact with the membrane, these
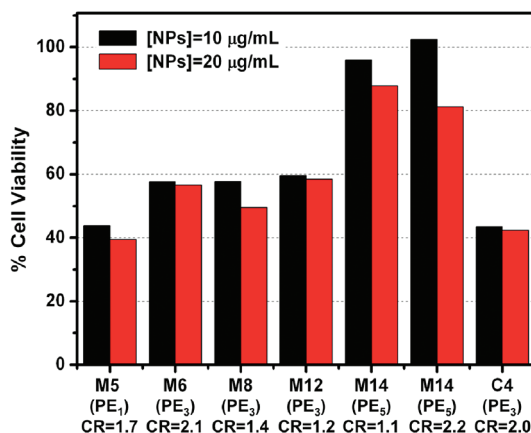

Figure 7. Percentage of cell viability (cytotoxicity results) at two different concentrations (10 and 20 μg/mL) using magnetoplexes from samples M_5, M_6, M_8, M_{12}, M_{14}, and C_4.

magnetoplex aggregates stood outside the cell. This behavior justifies the cytoxicity results obtained, finding an increased level of cell survival due to the lack of proper interaction when using the magnetoplexes from sample M_{14}. Magnetoplexes from samples M_8 and M_{12} (with increased CR values) have, however, decreased the cell viability to values lower than 60%, and although most of the nanostructures have not reached the cytoplasm of the cell, there is, of course, some influence in the assays. Although the three samples were similarly biolabeled, there are differences besides CR not being considered, such as the number of polyelectrolyte layers (three in the case of M_8 and M_{12} and five in the case of M_{14}), that definitively govern the level or type of aggregation and could therefore justify the differences in cell viability. Figure 8a includes a TEM image of magnetoplexes from sample M_{14} (CR = 1.1), where one can appreciate the aggregated nanostructures outside the Caco-2 cells.

The magnetoplexes with CR > 1.5 were able to internalize the cells and were exclusively found in endosomal compartments. However, in view of the very different results in terms of cytotoxicity values also summarized in Figure 7, the uptake pathways undergone seem to be different. All the assays where these magnetoplexes were employed offer very different percentages of cell viability (below 40% (M_5 and C_4), below 60% (M_6), and above 80% (M_{14})). In these cases, the main difference in the samples corresponds again to the number of polyelectrolytes deposited before the DNA loading. The cytotoxicity seems to decrease upon increasing the number of polyelectrolytes because M_5 has one layer, M_6 and C_4 have three layers, and M_{14} has five layers. Although sample C_4 has three layers, the highest cytotoxicity values can be explained in terms of the magnetic material and likely the release of the much more toxic cobalt ions.

To rule out any possible effect or synergy of the biomolecules attached, we also carried out an extensive
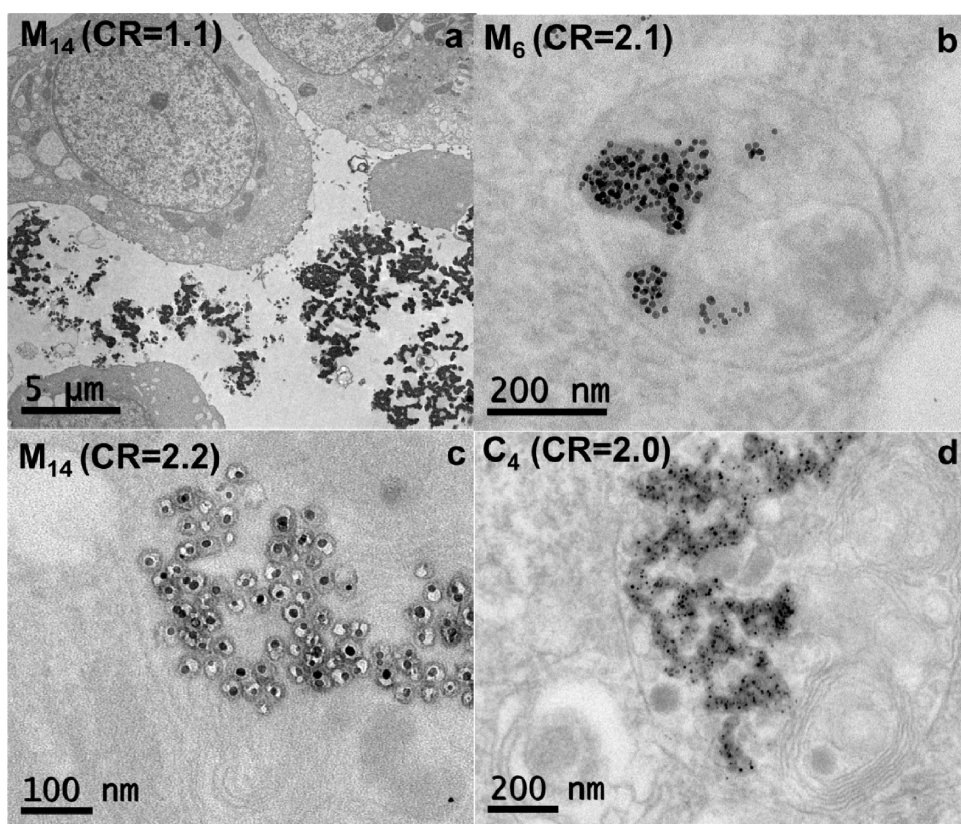
Figure 8. TEM images of magnetoplexes (with different values of CR) from samples M$_{14}$, M$_6$, and C$_4$ after interacting with Caco-2 cells.

TEM analysis of the nanoparticles taken up inside the cells. Interestingly, the TEM analysis indicates that these magnetoplexes with increased CR appear to be very susceptible to degradation, but again depending on the number of polyelectrolytes. The polyelectrolyte film and the DNA compaction responds differently to the lower pH conditions encountered in the intracellular environment. Figure 8b, c, and d show TEM images of the magnetoplexes with CR > 1.5 from samples M$_6$, M$_{14}$, and C$_4$ ingested inside the endosomes. Those from sample M$_{14}$ appear as individual, while those from samples M$_6$ and C$_4$ have evolved into a silica matrix with the magnetic nanoparticles trapped inside. Again, there are no big differences between the magnetoplexes unless we consider the subtle divergences in CR and the number of polyelectrolytes. But interestingly, the cytotoxicity assays jointly with the TEM analysis indicate that the magnetoplexes appear to be or less susceptible to degradation, indicating that the biocoating can be stable enough to somehow shield the magnetic cores from the cellular environment. The average diameter of the magnetic cores from all the samples checked seems to remain invariable after the degradation process undergone when inside cells (Figure 8b, c, and d). The silica shell around every magnetic core has however undergone completely different changes in morphology. Indeed, the silica from samples M$_6$ and C$_4$ has evolved into gel networks

due to the lower pH encountered inside the endosomes. Nonetheless, the morphology attained by the silica shells in the magnetoplexes from sample M$_{14}$ is completely different. The TEM analysis reflects an etching process occurring primarily at the inner silica in contact with the magnetic material. The silica shell can become sufficiently etched, allowing the magnetic core to freely move in the void formed. Similar silica etching has been already reported.[48,49] The main difference in these cases compared to the present one is the use of APS (3-aminopropyltrimethoxysilane) in the silica network. Silicate bonds formed from APS are less cross-linked than silicate bonds formed from TEOS, and consequently, the APS-rich matrix is more porous and less dense and reacts faster. Since APS has not been used in our case, the reason for the inner etching may be related to the presence of the polyelectrolytes and the DNA fragments at the surface, but because all the samples analyzed have polyelectrolytes and DNA, only the increased number of polyelectrolytes (5) and the lesser amount of DNA (to reach the highest CR (2.2)) seem to make a difference here. Yin *et al.* reported a permeable silica shell through a surface-protected etching, an approach that can convert dense coatings into porous shells while still acting as physical barriers preventing the aggregation of the particles.[50] Analogously, the right combination of polyelectrolytes and DNA fragments can effectively protect the MSN surface

from dissolution inside the cells. Their polymeric chains containing multiple $-NH_2$ binding groups interact with the hydroxide groups, cross-linking the silica shell near the surface and increasing their stability against etching. The relatively large size of the polyelectrolytes used restricts their electrostatic interactions to take place only at the surface and consequently means negligible infiltration and ensures the protection only in the outer part of the silica shell. Since, again, all the magnetoplexes employed have PDADMAC in direct contact with the silica shell, there should be some kind of influence of the extra layers of polyelectrolytes deposited in the case of sample M_{14}.

Taking into account that the nanoparticles and magnetoplexes were all routed along the same endocytosis pathway, the differences observed in cellular behavior were not caused by a different localization of the magnetic nanostructures but by the physicochemical properties at their surface. The unique physicochemical properties of the magnetoplexes modified as a function of the number of polyelectrolyte layers and the DNA fragments (CR) solve the conundrum of achieving lower or higher values of cytotoxicity in analogous experiments.

It has been demonstrated that the kinetics of iron oxide NP degradation strongly depend on the nanoparticles' surface coating,[51] and in the case of silica-coated nanoparticles, De Cuyper *et al*. have reported their chemical instability once internalized into cells.[52]

Although the degradation of the silica shell to liberate monomers is in itself harmless, when it results in exposure of the spinel core to the acidic environment, toxic effects are induced, especially in the case of the intrinsically toxic cobalt ions composing the cobalt ferrite cores, which results in elevated toxicity upon dissolution. Nonetheless, the ability of some of the magnetoplexes to be internalized by the Caco-2 cells maintaining an acceptable cell survival percentage must be related to the way some mechanisms proceed, such as the silica dissolution or the likely Fe or Co cation release, and the number of polyelectrolytes and the CR definitively play important roles.

CONCLUSION

We have developed a method to tune the physicochemical properties of magnetic silica nanoparticles through the molecules chemisorbed to their surface that control the ζ-potential. This tuning of the physicochemical properties appears reflected in cytotoxicity values and in how and where the nanoparticles ended up inside or outside the cells. This response appears to be directly dependent on the molecules grafted at the surface, which determines the final charge ratio (modified in this case as a function of the number of layers of polyelectrolytes and DNA fragments). Hence, we conclude that the surface functionalization plays a key role not only in regulating the cell-membrane penetration but also in interfering with the cell activity.

EXPERIMENTAL SECTION

Chemicals. Ammonium hydroxide solution, NH_4OH (28—30% NH_3), and iron(III) chloride hexahydrate ($FeCl_3$, 97%) were obtained from Fluka. Oleic acid, iron acetylacetonate ($Fe(acac)_3$), dioctyl ether, iron pentacarbonyl ($Fe(CO)_5$), 1,2-hexadecandiol, oleylamine, benzyl ether, cobalt acetylacetonate ($Co(acac)_2$), cobalt(II) chloride hexahydrate ($CoCl_2 \cdot 6H_2O$, 98%), iron(III) nitrate nonahydrate ($Fe(NO_3)_3$, 98%), nitric acid (HNO_3, 65%), poly-(5)oxyethylene-4-nonylphenyl ether (NP-5), tetraethylorthosilicate (TEOS), poly(sodium 4-styrenesulfonate) (PSS) ($M_w \approx 70\,000$), poly(diallyldimethylamonium chloride) (PDADMAC) ($M_w < 200\,000$), phosphotungstic acid solution (10 vol %), sodium silicate, sodium chloride, sodium hydroxide, hexane, cyclohexane, and sodium salt of calf thymus DNA (2700 base pairs per fragment on average) were supplied from Sigma-Aldrich. Chloroform was supplied by Merck. All chemicals were used as received. Distilled water was deionized using a Millipore system (with conductivity lower than $18\ \mu S\ cm^{-1}$). The Caco-2 human colon adenocarcinoma cell line was obtained from the European Collection of Cell Cultures (ECACC no. 86010202).

Synthesis of Fe_3O_4 Nanoparticles. Fe_3O_4 nanocrystals (6.6 nm) were synthesized as follows: $Fe(CO)_5$ (0.4 mL, 3.04 mmol) was injected under N_2 flow into a mixture containing 20 mL of octyl ether and 1.72 mL of oleic acid (5.42 mmol) at 100 °C, previously deoxygenated under N_2 for 20 min. The resulting mixture was slowly heated (280—290 °C) and refluxed for 2 h under an open atmosphere, observing a change of color from yellow to black. The solution was allowed to cool to room temperature under continuous magnetic stirring and subsequently treated with excess ethanol. The formed nanoparticles were separated by centrifugation, and the process was repeated at least three

times. Finally the Fe_3O_4 nanoparticles were dispersed in 30 mL of hexane solution, adding 20 μL of oleic acid.[53,54]

Fe_3O_4 nanocrystals (12.8 nm) were synthesized as follows: $Fe(acac)_3$ (3 mmol) was added to a mixture of 1,2-hexadecanediol (10 mmol), oleic acid (6 mmol), oleylamine (6 mmol), and octhyl ether (286—287 °C) (20 mL) under magnetic stirring and N_2 flow. The mixture was heated to 290 °C for 1 h and allowed to reflux (2 h). Again, a change of color from yellow to black was observed.[55] The formed nanoparticles were separated by centrifugation, adding ethanol, and the process was repeated at least three times. Finally the Fe_3O_4 nanoparticles were dispersed in 30 mL of hexane solution, adding 20 μL of oleic acid.

Fe_3O_4 nanocrystals (15 nm) were synthesized as follows: $Fe(acac)_3$ (2 mmol), 1,2-hexadecanediol (10 mmol), benzyl ether (20 mL), oleic acid (2 mmol), and oleylamine (2 mmol) were mixed and magnetically stirred under N_2 flow. A volume (0.3 mL) of hexane with 6.6 nm Fe_3O_4 nanocrystals as synthesized was then added. The mixture was first heated to 100 °C and then to reflux for 1 h more.[56] The black-brown mixture was cooled to room temperature. Under ambient conditions, ethanol (40 mL) was added to the mixture, and a black material was precipitated and separated *via* centrifugation. The black product was redispersed in 40 mL of hexane, simultaneously adding oleic acid (0.05 mL) and oleylamine (0.05 mL).

Synthesis of $CoFe_2O_4$ Nanoparticles. *$CoFe_2O_4$ Nanoparticles in Aqueous Solution (ref 57).* Solutions of 5 mL of 2 M $CoCl_2 \cdot 6H_2O$ in HCl 7.4% and 40 mL of 0.5 M $FeCl_3 \cdot 6H_2O$ in Milli Q water were prepared. Both solutions were taken to 50 °C, mixed, and poured into a boiling solution of 200 mL of 1 M NaOH under vigorous stirring. The boiling was maintained for 30 min, and the solution was cooled to room temperature without stirring.

After five water-cleaning stages by magnetic sedimenting and decanting of the supernatant, the ferrofluid is treated with an oxidative reaction to passivate the surface. For that, the nanoparticles were dispersed in 30 mL of a 2 M HNO$_3$ solution with 0.35 M Fe(NO$_3$)$_3$·9H$_2$O and heated to 100 °C for 45 min with continuous stirring. The resulting product was magnetically sedimented overnight. Then the supernatant was decanted and substituted with 100 mL of Milli Q water.

CoFe$_2$O$_4$ Nanoparticles in Organic Solution. CoFe$_2$O$_4$ nanoparticles were prepared by adding Fe(acac)$_3$ (2 mmol) and Co(acac)$_2$ (1 mmol) to a mixture containing 1,2-hexadecanediol (10 mmol), oleic acid (6 mmol), oleylamine (6 mmol), and benzyl ether (20 mL) under magnetic stirring and N$_2$ flow. The mixture was heated to 200 °C for 2 h and then to reflux (300 °C) for 1 h.[58] The resulting black mixture was cooled to room temperature and washed and dispersed in 30 mL of hexane, adding 20 μL of oleic acid, analogously to the Fe$_3$O$_4$ nanoparticles.

Synthesis of Magnetic Silica Nanoparticles. For incorporation in silica, the Fe$_3$O$_4$ and CoFe$_2$O$_4$ nanoparticles were transferred to chloroform or cyclohexane (in the case of nanoparticles synthesized in aqueous solution by adding oleic acid for the phase transfer). For a typical reverse microemulsion synthesis,[21] 1.3 mL of NP-5 was dispersed in 10 mL of cyclohexane and stirred for 15 min. Subsequently, Fe$_3$O$_4$ or CoFe$_2$O$_4$ nanoparticles dispersed in chloroform (100−200 μL, 0.05M) were added, after which different volumes (20−150 μL, depending on the final silica shell thickness) of TEOS and 850 μL of ammonia hydroxide solution were added. These conditions varied in the case of the cobalt ferrite nanoparticles synthesized in aqueous solutions. For their coating, 2.6 mL of NP-5 was dispersed in 13 mL of cyclohexane and stirred for 15 min. Subsequently, the 21.5 nm CoFe$_2$O$_4$ nanoparticles now dispersed in cyclohexane (6 mL, ∼0.18 mM) were added, after which different volumes (10−25 μL, depending on the final silica shell thickness) of TEOS and 300 μL of ammonia hydroxide solution were added.

For all the samples, between the additions, the reaction mixture was stirred for 15 min. After the last step, the mixture was stirred for 1 min and then stored at room temperature for 1 week. Finally, the silica-coated magnetite or cobalt ferrite nanoparticles were purified (by adding ethanol to the reaction mixture for centrifugation (10 min, 1800g)) and redispersed in water.

Surface Modification of the MSNs. A polyelectrolyte film was deposited by the alternate adsorption of PDADMAC (poly-(diallyldimethylammonium chloride)), PSS (poly(sodium 4-styrenesulfonate)) and PDADMAC onto the MSNs as indicated elsewhere,[39] in such a way that the polymer selected has an charge opposite that on the silica spheres, hence predominantly adsorbing through electrostatic interactions. These polyelectrolyte-coated particles were prepared by adding 100 μL of concentrated suspension of MSNs (2.5 wt %) to a 1 mL solution of PDADMAC (1 mg mL^{-1}, containing 0.5 M NaCl), waiting 15 min for adsorption and then removing excess PDADMAC by four repeated centrifugation/wash cycles. The centrifugation was done with a relative centrifugal force of 3800g for 10 min. PSS (1 mg mL^{-1}, containing 0.5 M NaCl) was deposited onto PDADMAC-coated MSNs in a similar way using the same conditions, followed by the next PDADMAC layer. All the cases of one, three, or five layers of polyelectrolytes produce a smoother, more uniform and positively charged surface on the MSNs.

Preparation of Magnetoplexes (MSNs−DNA Complexes). A stock solution of calf thymus DNA (CT DNA) (0.073 mg/mL = 1.12 × 10^{-4} M base pairs) was prepared by dissolving an appropriate amount of the solid in aqueous solution two days before mixing with the PE$_n$-MSNs. DNA concentrations (expressed in mM base pairs) were determined by absorbance at 260 nm (ε = 6600 M^{-1} cm). A A_{260}/A_{280} ratio of 1.90 and a negligible absorbance at 320 nm (A_{320} = −0.003) reveal that the contamination of the DNA used in this work by the presence of a certain percentage of proteins is negligible.[59,60] Appropriate aliquots of the positively charged MSN suspensions were mixed with a 0.5 mL stock solution of CT DNA, whose concentration is kept constant, to cover a wide range of charge ratios (CR = moles of the MSNs' positive charges/mol of DNA negative charges) on the nanoparticle surface. Samples were then vortexed for 5 min.

Cytotoxicity Assays. The Caco-2 human colon adenocarcinoma cell line was used to evaluate cell viability in the presence of the different types of nanoparticles. Cells were routinely grown in 25 or 75 cm^2 plastic flasks in Dulbecco's modified Eagle's medium containing 4.5 g/L glucose, 10% fetal calf serum, 100 units/mL of penicillin, 100 μg/mL of streptomycin, 2 mM L-glutamine, and 1% nonessential amino acids at 37 °C, in a 5% CO$_2$ humidified atmosphere. Cytotoxicity was determined using a colorimetric assay with 3-(4,5-dimethylthiazol-2-yl)-2,5-diphenyltetrazolium bromide (MTT) reagent.[61,62] This assay is based on the conversion of the yellow tetrazolium salt to purple formazan crystals by metabolically active cells. In these experiments, cells were seeded at a density of 10 000 cells per well into 96-well tissue culture plates and grown for 24 h before adding the tested nanoparticles. These nanoparticles, previously diluted in culture medium without fetal bovine serum, were added to the wells at final concentrations of 10 and 20 μg/mL (determined by ICP (inductively coupled plasma) analysis), and cells were incubated for 24 h. After the incubation, 10 μL of the MTT reagent was added to each well and cells were incubated for an additional 4 h period to allow the cleavage of the MTT reagent by viable cell mitochondrial dehydrogenase. Afterward, 100 μL of the solubilization solution was added and plates were incubated overnight. The absorbance of the solubilized formazan product was then spectrophotometrically quantified in an ELISA microplate reader at 570 nm with the reference at 630 nm. All experiments were performed three times and in triplicates. The cell viability is expressed as a percentage according to the following formula:

$$\%\text{Cell Viability} = \frac{A_{c+n+m} - A_{n+m}}{A_{c+m}} \times 100$$

where A_{c+n+m} corresponds to the absorbance of the cells with nanoparticles present in the medium, A_{n+m} corresponds to the absorbance of the nanoparticles in the medium (no cells present), and A_{c+m} corresponds to the absorbance of cells in the medium (no nanoparticles). The cell viabilities were therefore measured as a function of the relative cell survival percentages when compared to nanoparticle-free cell control, and the data reported represent an average of three measurements in all cases.

Characterization. TEM measurements were performed on a Philips CM12 instrument operating at an acceleration voltage of 120 kV. Samples for TEM were prepared by placing a drop of the dispersions on a Cu grid, letting the liquid evaporate at room temperature in the case of nanoparticles. In the case of cells, a specific protocol for cell culture was developed by the microscopy unit at the University of Vigo (http://webs.uvigo.es/cactiweb/s_microe/pmme01.htm). ICP analysis was performed using a Perkin-Elmer Optima 4300 DV. To study the dc (direct current) magnetic properties using superconducting quantum interference device (SQUID) magnetometry the magnetic nanoparticles were precipitated and the dried sample was measured. The phase analysis light-scattering technique (Zeta PALS, Brookhaven Instrum. Corp., USA) was used to measure electrophoretic mobilities (and from it, ζ-potential) and particle hydrodynamic sizes. This interferometric technique uses phase analysis light scattering to determine the electrophoretic mobility of charged nanoparticle suspensions. Electrophoretic mobility data, each taken as an average over 50 independent measurements, were registered as a function of magnetoplex compositions (MSNs to DNA molar ratios), including the values for MSNs in the absence of DNA. UV−vis spectra were collected using a Shimadzu UV-3101PC UV−visible spectrometer over the range 200−1100 nm.

Supporting Information Available: This material is available free of charge via the Internet at http://pubs.acs.org.

Note Added after ASAP Publication: The version of this paper that was published December 19, 2011, did not include all of the author's corrections. The corrected version was published December 22, 2011.

REFERENCES AND NOTES

1. Moyano, D. F.; Rotello, V. M. Nano Meets Biology: Structure and Function at the Nanoparticle Interface. *Langmuir* **2011**, *27*, 10376–13085.

2. Salgueiriño-Maceira, V.; Correa-Duarte, M. A. Increasing the Complexity of Magnetic Core/Shell Structured Nano-composites for Biological Applications. *Adv. Mater.* **2007**, *19*, 4131–4144.

3. Rosensweig, R. E. Heating Magnetic Fluid with Alternating Magnetic Field. *J. Magn. Magn. Mater.* **2002**, *252*, 370–374.

4. Pankhurst, Q. A.; Connolly, J.; Jones, S. K.; Dobson, J. Applications of Magnetic Nanoparticles in Biomedicine. *J. Phys. D: Appl. Phys.* **2003**, *36*, R167–R181.

5. Sengupta, S.; Eavarone, D.; Capila, I.; Zhao, G.; Watson, N.; Kiziltepe, T.; Sasisekharan, R. Temporal Targeting of Tumour Cells and Neovasculature with a Nanoscale Delivery System. *Nature* **2005**, *436*, 568–572.

6. Sanhai, W. R.; Sakamoto, J. H.; Canady, R.; Ferrari, M. Seven Challenges for Nanomedicine. *Nat. Nanotechnol.* **2008**, *3*, 242–244.

7. Manea, F.; Houillon, F. B.; Pasquato, L.; Scrimin, P. Nano-zymes: Gold-Nanoparticle-Based Transphosphorylation Catalysis. *Angew. Chem., Int. Ed.* **2004**, *43*, 6165–6169.

8. Nel, A. E.; Mädler, L.; Velegol, D.; Xia, T.; Hoek, E. M. V.; Somasundaran, P.; Klaessig, F.; Castranova, V.; Thompson, M. Understanding Biophysicochemical Interactions at the Nano-Bio Interface. *Nat. Mater.* **2009**, *8*, 543–557.

9. Ashley, C. E.; Carnes, E. C.; Phillips, G. K.; Padilla, D.; Durfee, P. N.; Brown, P. A.; Hanna, T. N.; Liu, J.; Phillips, B.; Carter, M. B.; *et al.* The Targeted Delivery of Multicomponent Cargos to Cancer Cells by Nanoporous Particle-Supported Lipid Bilayers. *Nat. Mater.* **2011**, *10*, 389–397.

10. Conner, S. D.; Schmid, S. L. Regulated Portals of Entry into the Cell. *Nature* **2003**, *422*, 37–44.

11. Xia, T.; Rome, L.; Nel, A. Nanobiology: Particles Slip Cell Security. *Nat. Mater.* **2008**, *7*, 519–520.

12. Massignani, M.; LoPresti, C.; Blanazs, A.; Madsen, J.; Armes, S. P.; Lewis, A. L.; Battaglia, G. Controlling Cellular Uptake by Surface Chemistry, Size and Surface Topology at the Nanoscale. *Small* **2009**, *5*, 2424–2432.

13. Jiang, W.; Kim, B. Y. S.; Rutka, J. T.; Chan, W. C. W. Nano-particle-Mediated Cellular Response is Size-Dependent. *Nat. Nanotechnol.* **2008**, *3*, 145–150.

14. Nel, A.; Xia, T.; Madler, L.; Li, N. Toxic Potential of Materials at the Nanolevel. *Science* **2006**, *311*, 622–627.

15. Leroueil, P. R.; Hong, S.; Mecke, A.; Baker, J. R., Jr.; Orr, B. G.; Banaszak Holl, M. M. Nanoparticle Interaction with Biological Membranes: Does Nanotechnology Present a Janus Face? *Acc Chem. Res.* **2007**, *40*, 335–342.

16. Lovric, J.; Bazzi, H. S.; Cuie, Y.; Fortin, G. R. A.; Winnik, F. M.; Maysinger, D. Differences in Subcellular Distribution and Toxicity of Green and Red Emitting CdTe Quantum Dots. *J. Mol. Med.* **2005**, *83*, 377–385.

17. Verma, A.; Uzun, O.; Hu, Y.; Hu, Y.; Han, H.-S.; Watson, N.; Chen, S.; Irvine, D. J.; Stellaci, F. Surface Structure-Regulated Cell Membrane Penetration by Monolayer Protected Nanoparticles. *Nat. Mater.* **2008**, *7*, 588–595.

18. Poon, Z.; Chen, S.; Engler, A. C.; Lee, H.; Atas, E.; von Maltzahn, G.; Bhatia, S. N.; Hammond, P. T. Ligand-Clustered "Patchy" Nanoparticles for Modulated Cellular Uptake and *in Vivo* Tumor Targeting. *Angew. Chem., Int. Ed.* **2010**, *49*, 7266–7270.

19. Boeneman, K.; Prasuhn, D. E.; Blanco-Canosa, J. B.; Dawson, P. E.; Melinger, J. S.; Ancona, M.; Stewart, M. H.; Susumu, K.; Huston, A.; Medintz, I. L. Self-Assembled Quantum Dot-Sensitized Multivalent DNA Photonic Wires. *J. Am. Chem. Soc.* **2010**, *132*, 18177–18190.

20. Climent, E.; Martinez-Manez, R.; Sancenon, F.; Marcos, M. D.; Soto, J.; Maqueira, A.; Amoros, P. Controlled Delivery Using Oligonucleotide-Capped Mesoporous Silica Nano-particles. *Angew. Chem., Int. Ed.* **2010**, *49*, 7281–7283.

21. Koole, R.; van Schooneveld, M. M.; Hilhorst, J.; De Mello Donega, C.; Hart, D. C.; van Blaaderen, A.; Vanmaekelbergh, D.; Meijerink, A. On the Incorporation Mechanism of Hydrophobic Quantum Dots in Silica Spheres by a Reverse Microemulsion Method. *Chem. Mater.* **2008**, *20*, 2503–2512.

22. Morrish, A. H. *The Physical Principles of Magnetism*; IEEE Press: New York, 1991.

23. Sorensen, C. M. Magnetism. In *Nanoscale Materials in Chemistry*; Klabunde, K. J., Ed.; Wiley & Sons: New York, 2001.

24. Hatch, G. P.; Stelter, R. E. Magnetic Design Considerations for Devices and Particles Used for Biological High-Gradient Magnetic Separation (HGMS) Systems. *J. Magn. Magn. Mater.* **2001**, *225*, 262–272.

25. Rodríguez-Pulido, A.; Aicart, E.; Junquera, E. Electrochemi-cal and Spectroscopic Study of Octadecyltrimethylammo-nium Bromide/DNA Surfoplexes. *Langmuir* **2009**, *25*, 4402–4411.

26. Ewert, K.; Slack, N. L.; Ahmad, A.; Evans, H. M.; Lin, A. J.; Samuel, C. E.; Safinya, C. R. Cationic Lipid-DNA Complexes for Gene Therapy: Understanding the Relationship be-tween Complex Structure and Gene Delivery Pathways at the Molecular Level. *Curr. Med. Chem.* **2004**, *11*, 133–149.

27. Pozzi, D.; Caracciolo, G.; Caminiti, R.; De Sanctis, S. C.; Amenitsch, H.; Marchini, C.; Montani, M.; Amici, A. Toward the Rational Design of Lipid Gene Vectors: Shape Coupling between Lipoplex and Anionic Cellular Lipids Controls the Phase Evolution of Lipoplexes and the Efficiency of DNA Release. *Appl. Mater. Interfaces* **2009**, *1*, 2237–2249.

28. Muñoz-Ubeda, M.; Rodriguez-Pulido, A.; Nogales, A.; Martin-Molina, A.; Aicart, E.; Junquera, E. Effect of Lipid Composition on the Structure and Theoretical Phase Diagrams of DC-Chol/DOPE-DNA Lipoplexes. *Biomacro-molecules* **2010**, *11*, 3332–3340.

29. Dias, R. S.; Lindman, B. *DNA Interaction with Polymers and Surfactants*; Wiley & Sons: Hoboken, 2008.

30. Ahmad, A.; Evans, H. M.; Ewert, K.; George, C. X.; Samuel, C. E.; Safinya, C. R. New Multivalent Cationic Lipids Reveal Bell Curve for Transfection Efficiency Versus Membrane Charge Density: Lipid-DNA Complexes for Gene Delivery. *J. Gene Med.* **2005**, *7*, 739–748.

31. Bajaj, A.; Kondiah, P.; Bhattacharya, S. Design, Synthesis, and *in Vitro* Gene Delivery Efficacies of Novel Cholesterol-Based Gemini Cationic Lipids and Their Serum Compat-ibility: a Structure-Activity Investigation. *J. Med. Chem.* **2007**, *50*, 2432–2442.

32. Muñoz-Ubeda, M.; Rodriguez-Pulido, A.; Nogales, A.; Llorca, O.; Quesada-Perez, M.; Martin-Molina, A.; Aicart, E.; Junquera, E. Gene Vectors Based on DOEPC/DOPE Mixed Cationic Liposomes: A Physicochemical Study. *Soft Matter* **2011**, *5991*–6004.

33. Leal, C.; Bouxsein, N. F.; Ewert, K. K.; Safinya, C. R. Highly Efficient Gene Silencing Activity of siRNA Embedded in a Nanostructured Gyroid Cubic Lipid Matrix. *J. Am. Chem. Soc.* **2010**, *132*, 16841–16847.

34. Li, W.; Suez, I.; Szoka, F. C. Reconstitution of the M13 Major Coat Protein and Its Transmembrane Peptide Segment on a DNA Template. *Biochemistry* **2007**, *46*, 8579–8591.

35. Luo, D.; Saltzman, W. M. Synthetic DNA Delivery Systems. *Nat. Biotechnol.* **2000**, *18*, 33–37.

36. Zinchenko, A.; Sakaue, T.; Araki, S.; Yoshikawa, K.; Baigl, D. Single-Chain Compaction of Long Duplex DNA by Cationic Nanoparticles: Modes of Interaction and Comparison with Chromatin. *J. Phys. Chem. B* **2007**, *111*, 3019–3031.

37. Rosa, H.; Petri, D. F. S.; Carmona-Ribeiro, A. M. Interactions between Bacteriophage DNA and Cationic Biomimetic Particles. *J. Phys. Chem. B* **2008**, *112*, 16422–16430.

38. Koltover, I.; Salditt, T.; Radler, J. O.; Safinya, C. R. An Inverted Hexagonal Phase of Cationic Liposome-DNA Complexes Related to DNA Release and Delivery. *Science* **1998**, *281*, 78–81.

39. Kotov, N. A.; Dekany, I.; Fendler, J. H. Layer-by-Layer Self-Assembly of Polyelectrolytes-Semiconductor Nanoparticle Composite Films. *J. Phys. Chem.* **1995**, *99*, 13065–13069.

40. Caruso, F.; Caruso, R.; Möhwald, H. Nanoengineering of Inorganic and Hybrid Hollow Spheres by Colloidal Templating. *Science* **1998**, *282*, 1111–1114.

41. Caruso, F.; Lichtenfeld, H.; Giersig, M.; Möhwald, H. Electrostatic Self-Assembly of Silica Nanoparticle-Polyelectrolyte Multilayers on Polystyrene Latex Particles. *J. Am. Chem. Soc.* **1998**, *120*, 8523–8524.

42. Wang, Y.; Gao, S.; Ye, W.-H.; Yoon, H. S.; Yang, Y. Co-Delivery of Drugs and DNA from Cationic Core-Shell Nanoparticles Self-Assembled from a Biodegradable Copolymer. *Nat. Mater.* **2006**, *5*, 791–796.

43. Hayat, M. A. *Principles and Techniques of Electron Microscopy: Biological Applications*; Cambridge University Press, 2000.

44. Everett, M. M.; Miller, W. A. The Role of Phosphotungstic and Phosphomolibdic Acids in Connective Tissue Staining. *Histochem. J.* **1974**, *6*, 25–34.

45. Liu, S.; Kurth, D. G.; Bredenkötter, B.; Volkmer, D. The Structure of Self-Assembled Multilayers with Polyoxometalate Nanoclusters. *J. Am. Chem. Soc.* **2002**, *124*, 12279–12287.

46. Rodríguez-Pulido, A.; Ortega, F.; Llorca, O.; Aicart, E.; Junquera, E. A Physicochemical Characterization of the Interaction between DC-Chol/DOPE Cationic Liposomes and DNA. *J. Phys. Chem. B* **2008**, *112*, 12555–12565.

47. Wilhelm, C.; Gazeau, F. Universal Cell Labeling with Anionic Magnetic Nanoparticles. *Biomaterials* **2008**, *29*, 3161–3174.

48. Grzelczak, M.; Correa-Duarte, M. A.; Liz-Marzan, L. M. Carbon Nanotubes Encapsulated in Wormlike Hollow Silica Shells. *Small* **2006**, *2*, 1174–1177.

49. Roca, M.; Haes, A. J. Silica-Void-Gold Nanoparticles: Temporally Stable Surface-Enhanced Raman Scattering Substrates. *J. Am. Chem. Soc.* **2008**, *130*, 14273–14279.

50. Zhang, Q.; Zhang, T.; Ge, J.; Yin, Y. Permeable Silica Shell Through Surface-Protected Etching. *Nano Lett.* **2008**, *8*, 2867–2871.

51. Levy, M.; Lagarde, F.; Maraloiu, V.-A.; Blanchin, M.-G.; Gendron, F.; Wilhelm, C.; Gazeau, F. Degradability of Superparamagnetic Nanoparticles in a Model of Intracellular Environment: Follow-up of Magnetic, Structural and Chemical Properties. *Nanotechnology* **2010**, *21*, 395103–395114.

52. Soenen, S. J. H.; Himmelreich, U.; Nuytten, N.; Pisanic, T. R., II; Ferrari, A.; de Cuyper, M. Intracellular Nanoparticle Coating Stability Determines Nanoparticle Diagnostics Efficacy and Cell Functionality. *Small* **2010**, *6*, 2136–2145.

53. Hyeon, T.; Lee, S. S.; Park, J.; Chung, Y.; Na, H. B. Synthesis of Highly Crystalline and Monodisperse Maghemite Nanocrystallites without a Size-Selection Process. *J. Am. Chem. Soc.* **2001**, *123*, 12798–12801.

54. Woo, K.; Hong, J.; Choi, S.; Lee, H.-W.; Ahn, J.-P.; Kim, C. S.; Lee, S. W. Easy Synthesis and Magnetic Properties of Iron Oxide Nanoparticles. *Chem. Mater.* **2004**, *16*, 2814–2818.

55. Sun, S.; Zeng, H. Size-Controlled Synthesis of Magnetite Nanoparticles. *J. Am. Chem. Soc.* **2002**, *124*, 8204.

56. Sun, S.; Zeng, H.; Robinson, D.; Raoux, B. S.; Rice, P. M.; Wang, S. X.; Li, G. Monodisperse MFe_2O_4 (M = Fe, Co, Mn) Nanoparticles. *J. Am. Chem. Soc.* **2004**, *126*, 273.

57. Wagner, J.; Autenrieth, T.; Hempelmann, R. Core Shell Particles Consisting of Cobalt Ferrite and Silica as Model Ferrofluids. *J. Magn. Magn. Mater.* **2002**, *252*, 4–6.

58. Dai, Q.; Lam, M.; Swanson, S.; Yu, R.-H. R.; Milliron, D. J.; Topuria, T.; Juber, P.-O.; Nelson, A. Monodisperse Cobalt Ferrite Nanomagnets with Uniform Silica Coatings. *Langmuir* **2010**, *26*, 17546–17551.

59. Mel'nikov, S. M.; Lindman, B. Solubilization of DNA-Cationic Lipid Complexes in Hydrophobic Solvents. A Single-Molecule Visualization by Fluorescence Microscopy. *Langmuir* **1999**, *15*, 1923–1928.

60. Barreleiro, P. C. A.; Lindman, B. The Kinetics of DNA-Cationic Vesible Complex Formation. *J. Phys. Chem. B* **2003**, *107*, 6208–6213.

61. Mosmann, T. Rapid Colorimetric Assay for Cellular Growth and Survival: Application to Proliferation and Cytotoxicity Assays. *J. Immunol. Methods* **1983**, *65*, 55–63.

62. García-Lorenzo, A.; Tojo, E.; Tojo, J.; Teijeira, M.; Rodríguez-Berrocal, F. J.; Pérez González, M.; Martínez-Zorzano, V. S. Cytotoxicity of Selected Imidazolium-Derived Ionic Liquids in the Human Caco-2 Cell Line. Sub-Structural Toxicological Interpretation through a QSAR Study. *Green Chem.* **2008**, *10*, 508–516.